JOURNAL OF SYNCHROTRON RADIATION

ISSN 1600-5775

The potential benefits of using higher X-ray energies for macromolecular crystallography

Joshua L. Dickerson and Elspeth F. Garman*

Department of Biochemistry, University of Oxford, South Parks Road, Oxford OX1 3QU, UK.
*Correspondence e-mail: elspeth.garman@bioch.ox.ac.uk

Received 1 February 2019
Accepted 1 May 2019

Edited by M. Weik, Institut de Biologie Structurale, France

Keywords: radiation damage; incident X-ray energies; dose; photoelectron escape.

Supporting information: this article has supporting information at journals.iucr.org/s

Using X-ray energies higher than those normally used (5–15 keV) for macromolecular X-ray crystallography (MX) at synchrotron sources can theoretically increase the achievable signal as a function of dose and reduce the rate of radiation damage. In practice, a major stumbling block to the use of higher X-ray energy has been the reduced quantum efficiency of silicon detectors as the X-ray energy increases, but hybrid photon-counting CdTe detectors are optimized for higher X-ray energies, and their performance has been steadily improving. Here the potential advantages of using higher incident beam energy together with a CdTe detector for MX are explored, with a particular focus on the advantages that higher beam energies may have for MX experiments with microbeams or microcrystals. Monte Carlo simulations are presented here which for the first time include the efficiency responses of some available X-ray detectors, as well as the possible escape of photoelectrons from the sample and their entry from surrounding material. The results reveal a 'sweet spot' at an incident X-ray energy of 26 keV, and show a greater than factor of two improvement in diffraction efficiency at this energy when using microbeams and microcrystals of 5 µm or less.

1. Introduction

X-ray crystallography of cryo-cooled samples at synchrotron sources remains the premier method for high-resolution protein structure determination. Historically, most macromolecular crystallography (MX) experiments were carried out at copper target home sources using the Cu K_α wavelength of 1.5418 Å. Most MX experiments are now performed at synchrotron sources with preferred X-ray wavelengths of around 1 Å (∼12.4 keV). Shorter-wavelength photons have the advantage of having less chance of being absorbed by the sample since the probability of photoelectric absorption decreases (see Fig. 1), making experimental absorption corrections negligible. These wavelengths can also exploit anomalous scattering for phase determination since they are close to the selenium *K*-absorption edge (λ = 0.98 Å) and the *L*-absorption edge of the heavy atom derivatives Pt, Au and Hg. At these wavelengths, there will also still be some anomalous signal from S (f'' = 0.242 at λ = 1 Å) and from any P (f'' = 0.185 at λ = 1 Å) if present, which can be used to improve phases.

A recent survey of all structures in the Protein Data Bank (PDB) determined by X-ray crystallography methods revealed that only about 0.7% of them were performed at incident X-ray wavelengths (λ_{inc}) shorter than 0.8 Å and only approximately 0.9% were conducted at a wavelength longer than 1.6 Å (Weiss, 2017).

In spite of these statistics, there are numerous reasons why using X-ray wavelengths outside this range might be advan-

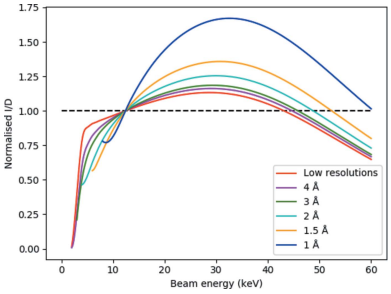

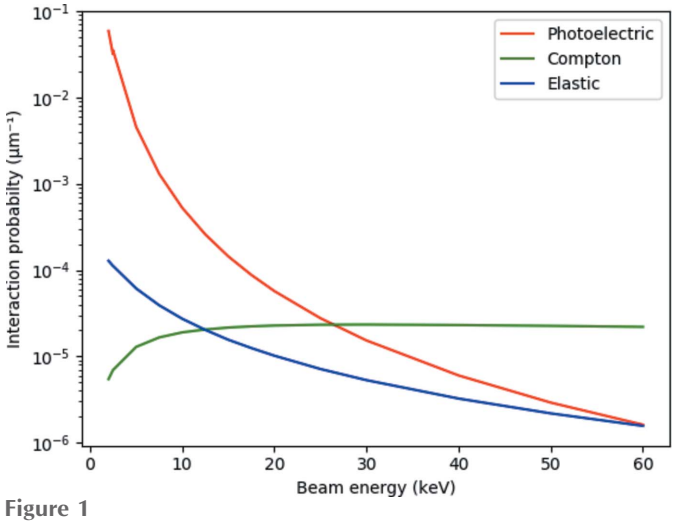

Figure 1
The probability of different types of interactions of X-rays with the crystal as a function of incident beam energy. The interaction probability, plotted using a logarithmic scale, is the reciprocal of the mean free path length for that interaction. The coefficients were calculated using the program *RADDOSE-3D* (Zeldin *et al.*, 2013; Bury *et al.*, 2018) for a lysozyme crystal (PDB 1dpx).

tageous. The primary rationale for considering using longer wavelengths (*i.e.* decreasing the incident energy, $E_{\rm inc}$) is to increase the anomalous signal from biologically relevant sulfur and phosphorus atoms and improve phasing without the use of heavy atom derivatives. The proof-of-principle experiments for this were conducted by Stuhrmann *et al.* (Lehmann *et al.*, 1993; Stuhrmann *et al.*, 1995, 1997). Mueller-Dieckmann *et al.* (Mueller-Dieckmann *et al.*, 2005) determined that the optimum wavelength to maximize the anomalous signal-to-noise ratio is 2.1 Å (5.904 keV), and that this is almost independent of the nature of the anomalously scattering substructure provided that there is no absorption edge near this wavelength. At this wavelength, there is a 300% increase in S f'' and a 310% increase in P f'' compared with at a $\lambda_{\rm inc}$ of 1 Å. A wavelength of around 2 Å is also closer to the *K*-edge of first-row transition metal atoms. The reader is directed to reviews by Carugo *et al.* (Carugo *et al.*, 2005) and Weiss (Weiss, 2017) for a more in depth discussion on the use of longer wavelengths.

The disadvantages of using longer X-ray wavelengths include: the greater importance of absorption corrections, an increase in the background noise on the detector due to more scattering of X-rays from air in the beam path [which can be mitigated by using a dedicated in-vacuum or in-helium beamline (Wagner *et al.*, 2016; Aurelius *et al.*, 2017; Liebschner *et al.*, 2016)] and, at wavelengths longer than ∼2–3 Å, the maximum resolution can become diffraction limited. Another issue is the reduction in the amount of signal obtained per unit of dose. Radiation damage is thought to be only dependent on absorbed dose (Gy = J kg^{-1}) (§2), and hence this is used to represent the extent of damage. This dose is a result of, firstly, photoelectric absorption of some X-rays with the concomitant emission of a photoelectron and either an Auger electron or a fluorescent X-ray, and, secondly, X-ray energy loss due to Compton (inelastic) scattering (see Fig. 1 for interaction probabilities as a function of $E_{\rm inc}$). The signal will be proportional to the number of elastically scattered photons, and diffraction efficiency (DE) is defined as the total number of photons elastically scattered by the crystal per MGy of absorbed dose. The signal can also be estimated from the predicted spot intensity. The relationship between the square of the structure factor, *F*, and the integrated spot intensity, *I*, is given by Darwin's formula (Darwin, 1914, 1922; Holton & Frankel, 2010),

$$I = I_{\rm beam}\, r_{\rm e}^2\, \frac{V_{\rm xtal}}{V_{\rm cell}}\, \frac{\lambda^3 L}{\omega V_{\rm cell}}\, PA\, |F|^2, \qquad (1)$$

where $I_{\rm beam}$ is the incident beam intensity, $r_{\rm e}$ is the classical electron radius, $V_{\rm xtal}$ is the crystal irradiated volume, $V_{\rm cell}$ is the unit-cell volume, *L* is the Lorentz factor which accounts for how the integrated spot intensity will be higher the slower the reflection moves through the Bragg condition, ω is the crystal angular velocity, *A* is the X-ray transmittance, and *P* is the polarization factor which accounts for reduced scattering when the incident beam and scattered beam **E**-vectors do not line up. When divided by dose, *D*, and terms which are independent of beam energy are removed, equation (1) becomes

$$\frac{I}{D} = \frac{\lambda^3 LP \exp(-\mu t)}{D}, \qquad (2)$$

where $A = \exp(-\mu t)$, with *t* being the thickness of the crystal and μ being the attenuation coefficient.

Given that radiation damage is thought to be only dependent on dose (§2), maximizing the DE and *I*/*D* will maximize the information obtained before the sample is compromised by radiation damage. This is particularly important for radiation-sensitive samples, such as metalloproteins, and small crystals for which the diffraction signal is weak. DE is one of the metrics output by the program *RADDOSE-3D* (Zeldin *et al.*, 2013; Bury *et al.*, 2018), a program used to calculate the spatially and temporally resolved dose absorbed by a rotating or stationary crystal during MX experiments. In *RADDOSE-3D*, the dose used to calculate DE is the diffraction weighted dose (DWD), an average dose which is weighted by how much flux each volume of the crystal receives. An increase in wavelength from 1 Å (12.398 keV) to 2.1 Å (5.904 keV) results in an approximately 50% reduction in DE for a crystal containing only organic atoms (Fig. 2) due to a large increase in the photoelectric cross section (Fig. 1) at longer wavelengths.

It can be seen by examining the DE normalized to the value at 12.4 keV that it does not vary with crystal size when the dose calculation neglects the probability of escape from the crystal of photoelectrons or fluorescent X-rays. However, the crystal composition (*e.g.* presence of heavy atoms) can slightly affect the DE since the photoelectric absorption cross section will increase just above *K*-shell absorption edges. This is illustrated in Fig. 3, where it can be seen that, for a holoferritin crystal containing approximately one Fe atom per two amino acids, there is a sudden drop in DE above the Fe *K*-edge

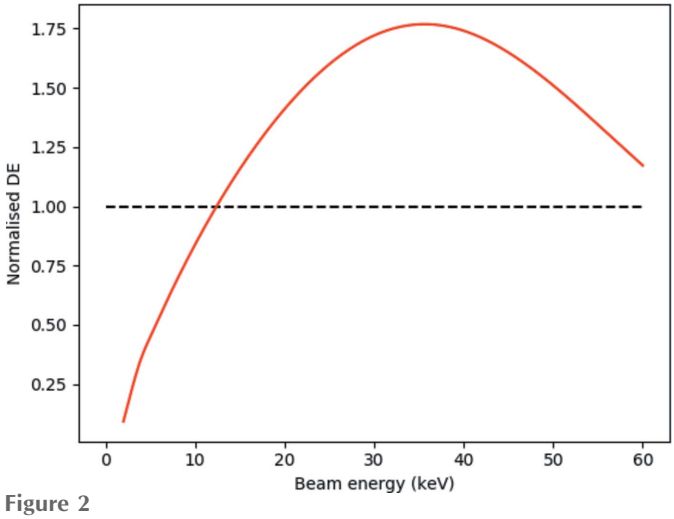

Figure 2
Diffraction efficiency (DE, the number of elastically scattered photons per MGy of absorbed dose), normalized to the value at 12.4 keV, as a function of incident beam energy for a protein crystal containing no atoms heavier than sulfur of the 91 kDa GH7 family cellobiohydrolase (PDB 5mcc) (Bury *et al.*, 2017). DE was calculated using the program *RADDOSE-3D* with no photoelectron or fluorescent escape from the crystal. There is a 1.76-fold increase in DE at 35 keV compared with that at 12.4 keV.

(7.112 keV) as a result of an increase in dose due to the increased photoelectric absorption cross section.

The main rationale for using shorter X-ray wavelengths is the increase in DE and *I*/*D* it can offer. Following a publication advocating the advantages of short-wavelength X-ray sources by Helliwell & Fourme (1983), Arndt (Arndt, 1984) gave a theoretical analysis of how various parameters affect the energy absorbed as a function of beam energy. Helliwell *et al.* (1993) expanded on this discussion and gave an account of the experimental potential for realizing MX at short incident wavelengths. Arndt used a similar metric to *I*/*D*, which he called I_E, and defined as the intensity for a given amount of absorbed energy. I was calculated only for low-resolution reflections with small Bragg angles, θ, where $\sin 2\theta \cong 2 \sin \theta$. For this case, the product of the Lorentz and polarization factors becomes approximately 1/λ. Arndt calculated a 1.09- and 1.13-fold increase in I_E on reducing the X-ray wavelength from 1.54 Å (8.05 keV) to 1.10 Å (11.3 keV) and 0.71 Å (17.5 keV), respectively. The same method for calculating I was used by Paithankar & Garman (2010), but absorbed energy was replaced with dose, and the original less sophisticated *RADDOSE-v3* was used to calculate the dose. A peak in *I*/*D* at 24–34 keV was obtained, with an approximately 1.2-fold improvement over the value at 12.4 keV. This range is similar to the peak DE of ∼35 keV (∼0.35 Å) evident in Fig. 2.

The shape shown in Fig. 2 arises because the photoelectric absorption cross section falls at a faster rate than does the elastic scattering cross section as $E_{\rm inc}$ increases from 2 to 35 keV. The Compton scattering cross section increases with beam energy and becomes larger than the photoelectric cross section above ∼27 keV (Fig. 1), accounting for the decrease in DE above ∼35 keV. There is a 1.76-fold improvement in DE from 12.4 keV to 35 keV in Fig. 2, higher than that calculated by Paithankar & Garman. To determine whether this difference arises from the fact that Paithankar & Garman only considered small Bragg angles, the data in Fig. 2 were converted to *I*/*D* for different resolutions (Fig. 4). The average product of Lorentz and polarization factors for a full rotation, *LP*, was calculated with the following equation,

$$LP\, f_{\rm obs} = \frac{\pi(3 + \cos 4\theta)}{16 \sin \theta}, \qquad (3)$$

where $f_{\rm obs}$ is the fraction of all reflections at a given resolution that cross the Ewald sphere when rotating about a single axis

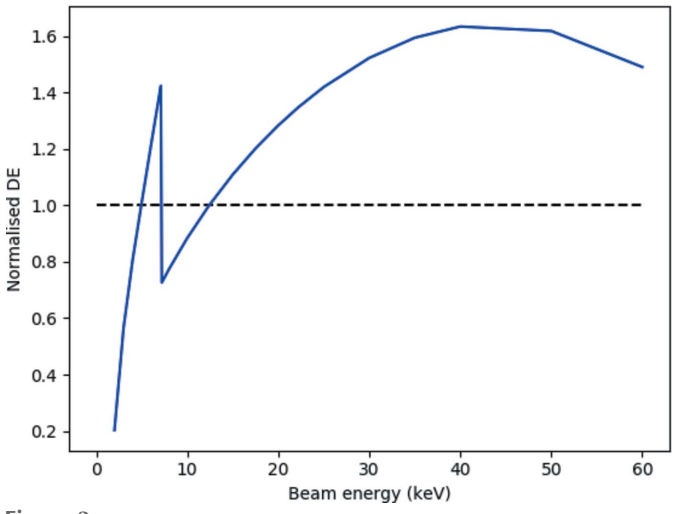

Figure 3
DE, normalized to the value at 12.4 keV, as a function of beam energy for holoferritin crystals, which contain approximately one Fe ion for every two amino acids. DE was calculated using the program *RADDOSE-3D* with no photoelectron or fluorescent escape from the crystal. The downward step at 7.1 keV is at the Fe *K*-edge.

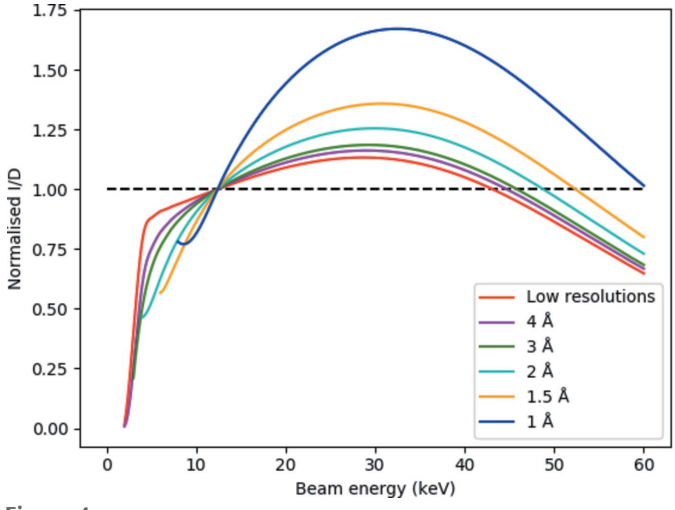

Figure 4
I/*D* [equations (2) and (3)] normalized to the value at 12.4 keV as a function of incident beam energy for a protein crystal of the 91 kDa GH7 family cellobiohydrolase (PDB 5mcc) (Bury *et al.*, 2017) which contains no atoms heavier than sulfur. The dose was calculated using the program *RADDOSE-3D* with no photoelectron or fluorescent escape from the crystal. The higher the resolution of the reflection, the bigger the improvement in *I*/*D* on increasing the beam energy, with a 1.66-fold increase from 12.4 keV to 35 keV for 1 Å reflections.

(Holton & Frankel, 2010). From Fig. 4, it can be seen that increasing the incident beam energy has a greater effect on higher-resolution shells, with a 1.66-fold increase from 12.4 keV to 35 keV for 1 Å reflections.

Other advantages of using a higher E_{inc} include: a further reduction in errors due to lower absorption by the crystal, reduced curvature of the Ewald sphere (beneficial for data completeness), and the ability to move the detector further away from the sample for the same maximum resolution. Having more distance, x, between the sample and detector allows more room for devices, such as a diamond anvil cell for high-pressure MX, a UV-vis optical microspectrophotometer, a larger and shorter goniometer for increased stability or a smaller (*i.e.* cheaper) detector.

However, as the energy is increased, the reduction in elastic scattering cross sections will reduce the percentage of elastically scattered photons. This would have little impact on conventional MX, since simply using longer exposure times will increase the number of elastically scattered photons.

A clear disadvantage of using shorter X-ray wavelengths is the reduction in anomalous signal from S and P. A wavelength of 0.5 Å (24.797 keV) has an f'' that is approximately 25% of that at 1 Å (12.398 keV) for both S and P. Thus lower beam energies are required to allow phasing from anomalous S and P signals [*e.g.* beamline I23 at Diamond Light Source which is optimized to operate between 1.5 and 4 Å (Wagner *et al.*, 2016)]. However, it should be noted that phasing at short wavelengths utilizing other scatterers has been successful in several studies, notably to solve the structure of porcine pancreatic elastase to 1.8 Å resolution at an incident energy of 34.59 keV. A bound xenon atom (*K*-edge 0.358 Å, 34.59 keV) allowed single isomorphous replacement with anomalous scattering (SIRAS) phasing (Schiltz *et al.*, 1997). Subsequently, multi-wavelength anomalous dispersion (MAD) experiments at 35 keV successfully led to the determination of the structure of chicken egg-white lysozyme (CEWL) to 1.6 Å, firstly with bound iodine (*K*-edge 33.17 keV) and secondly with Xe (Takeda *et al.*, 2004). An even higher E_{inc} of nearly 56 keV was employed by Jakoncic *et al.* (2006) with SIRAS to solve CEWL to 1.25 Å using three bound holmium atoms (*K*-edge 55.618 keV) and the structure was of similar quality to one obtained at an E_{inc} of 12 keV.

Notwithstanding these successful 'proof of principle' experiments, a major issue with the use of higher E_{inc} for MX is the reduction in quantum efficiency (QE) of the detectors as E_{inc} is increased. The latest generation of detectors register X-rays directly by hybrid photon counting (HPC) through absorption of the photons by a sensor material, leading to the generation of electron–hole pairs and a charge that is collected, measured and processed. The most common sensor material used in HPC detectors at MX beamlines is silicon. The changes in QE with beam energy for various thickness silicon detectors are shown in Fig. 5. Even for a 1000 µm-thick silicon sensor, the QE drops sharply above an E_{inc} of 15 keV, and drops to below 50% above 22.1 keV.

However, other sensor materials, such as Ge, GaAs and CdTe, can provide better QE at E_{inc} incident beam energies

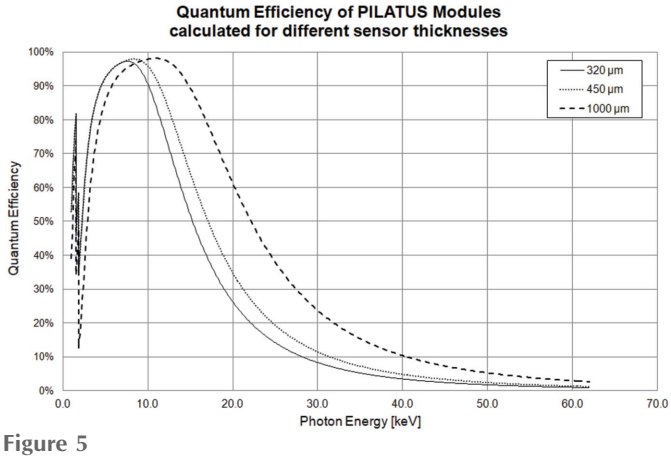

Figure 5
The variation with E_{inc} in the detector quantum efficiency of PILATUS detectors with silicon sensor material of different thicknesses (Donath *et al.*, 2013). The theoretical quantum efficiencies are the fraction of incident radiation that is calculated to be absorbed in the sensitive volume of the silicon sensor using mass attenuation coefficients from the NIST XCOM tables (Berger *et al.*, 1998). The falls in quantum efficiency at 1.839 keV and 1.560 keV are as a result of the silicon *K*- and L_I-absorption-edges, respectively.

above 15 keV, with large-area CdTe detectors now commercially available. Using cadmium telluride (CdTe) crystals instead of silicon increases the photoelectric absorption cross section and QE at higher beam energy (Fig. 6). At approximately E_{inc} = 15 keV, there is a crossover point where the QE of the CdTe sensor becomes higher than that of any available silicon sensors.

The quality of CdTe detectors has also been steadily improving due to progress in optimizing material quality and in processing. Typical grain boundaries and growth imperfections associated with CdTe crystals (Hatsui & Graafsma, 2015) have clearly been seen by many groups (Cecilia *et al.*, 2011; Ruat & Ponchut, 2012; Frojdh *et al.*, 2013), but better CdTe crystals and flat-field corrections have mitigated their detrimental effects (Purohit *et al.*, 2016). Another issue with these detectors is that the response of CdTe is known to vary

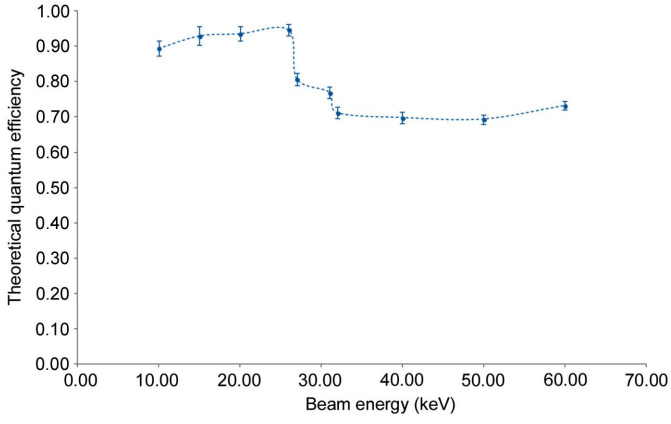

Figure 6
The theoretical quantum efficiency (QE) of 750 µm-thick EIGER CdTe detectors as a function of beam energy (Zambon *et al.*, 2018). The downward steps in QE at 26.7 keV and 31.8 keV are at the Cd and Te *K*-shell absorption edges, respectively.

as a function of time and exposure. These phenomena are termed polarization effects and are thought to be caused by trapping of charge carriers. Periodic reset procedures can remove the residual effects of previous illumination, but they need to be scheduled around measurements (Hatsui & Graafsma, 2015).

2. Does the incident beam energy affect the rate of radiation damage?

As mentioned previously, during MX data collection, X-rays deposit energy in the sample through the photoelectric effect and the Compton effect, causing damage to the sample. Absorbed dose is used as a reproducible '*x*-axis' to plot various metrics employed to monitor radiation damage. The ability to compare radiation damage rates between different experimental setups using dose relies on radiation damage being dependent only on the amount of energy absorbed (the dose) and being independent of factors such as the particular beam energy employed. It is therefore vital to establish that the rate of radiation damage is independent of $E_{\rm inc}$ before evaluating potential improvements in DE at higher incident beam energies.

There are two different ways in which radiation damage manifests itself: global damage and specific damage. Global radiation damage causes degradation of the crystal lattice, and can be seen in the diffraction pattern by gradual fading and loss of high-resolution reflections. Specific radiation damage, whose onset for cryocooled crystals is typically seen at much lower doses than global radiation damage, causes chemical changes within the asymmetric unit such as: reduction of metal ions, cleavage of disulfide bonds, and decarboxylation of aspartate and glutamate residues. For a more in-depth discussion on the causes and consequences of radiation damage, the reader is referred to reviews by Holton (2009) and Garman & Weik (2017).

Several studies on cryocooled crystals have concluded that the rate of global radiation damage on a dose axis is independent of beam energy (Liebschner *et al.*, 2015; Shimizu *et al.*, 2007; Fourme *et al.*, 2012) using various different metrics, including reduction in reflection intensity (Liebschner *et al.*, 2015), increase in average *B*-factors (Shimizu *et al.*, 2007; Fourme *et al.*, 2012) and, often, but not always, an increase in mosaicity (Shimizu *et al.*, 2007; Fourme *et al.*, 2012). However, there are conflicting results as to whether the rate of specific damage is independent of $E_{\rm inc}$. When comparing consecutive electron density maps derived from data collected from cryocooled crstals at different X-ray wavelengths, Weiss *et al.* (2005) and Shimizu *et al.* (2007) saw no dependence of specific damage on beam energy. However, Homer *et al.* (2011) saw an increased rate of disulfide bond cleavage at $E_{\rm inc}$ = 14 keV compared with at 9 keV, but they saw no difference in the rate of methionine S—C bond cleavage. Since these data were published, new tools have been created to aid the study of specific radiation damage. The program *RABDAM* (Shelley *et al.*, 2018) calculates the $B_{\rm Damage}$ metric, a per-atom metric that identifies sites of specific damage by deconvoluting the atomic *B*-factors from the local packing density, for all selected atoms in a PDB or mmCIF file. *RABDAM* also calculates the $B_{\rm net}$ metric, a derivative of $B_{\rm Damage}$ that summarizes the total extent of specific damage in a single value (Shelley & Garman, 2019). The program *RIDL* (Bury & Garman, 2018) outputs several per-atom metrics to describe the extent of specific radiation damage based on changes in Fourier difference maps and the change in electron density between successive datasets. These tools could be used to re-examine previous experiments to better quantify the extent of specific radiation damage and also aid new investigations to determine whether specific radiation damage is or is not independent of beam energy. If the reported increased rate of disulfide bond breakage for the same dose at higher beam energy is not artefactual, new mechanisms would need to be proposed and tested to explain this phenomenon.

3. A closer look at diffraction efficiency

For the results shown in Fig. 2, the calculation of DE assumed that the QE of the detector was 100%. As previously mentioned, the QE of detectors varies with photon energy and this effect must therefore be included to obtain a realistic comparison of DEs at different X-ray energies. The DEs for different detectors, neglecting the probability of photoelectron escape from the crystal, are shown in Fig. 7. The optimum beam energy to maximize DE is ∼12.4 keV for a 450 µm silicon sensor, ∼15 keV for a 1000 µm silicon sensor and ∼26 keV for a 750 µm CdTe detector. When using the detector with the highest QE for each beam energy, there is a 1.6-fold increase in DE at 26 keV (CdTe sensor) compared with at 12.4 keV (1000 µm silicon sensor). Above the Cd *K*-edge at 26.7 keV, the DE drops sharply due to a decrease in the CdTe detector QE.

To maximize the DE, these results suggest that the optimum $E_{\rm inc}$ for data collection is 26 keV provided a detector with a CdTe sensor is used. However, in the field of MX radiation damage, a factor of 1.6 is considered too small to be very noteworthy. Holton (2009) argues that for a radiation damage mitigation strategy to be considered significant, the difference should be at least a factor of two. The uncertainty in beam intensity and crystal volume can each be as much as a factor of two and therefore make changes in results that are smaller than this difficult to reliably measure experimentally. This, coupled with the reduced anomalous signal from S and P as $E_{\rm inc}$ increases, and imperfections in the CdTe detectors, mean that there is likely to be little advantage from increasing the incident beam energy from ∼12.4 keV when photoelectron escape from the crystal is not significant. For this reason some experimental studies have failed to find an increase in signal-to-background ratio on increasing $E_{\rm inc}$ (Gonzalez *et al.*, 1994).

4. Could higher beam energies be beneficial for smaller beams and smaller crystals?

Higher beam energies have the potential to further increase the DE relative to $E_{\rm inc}$ = 12.4 keV when the probability of

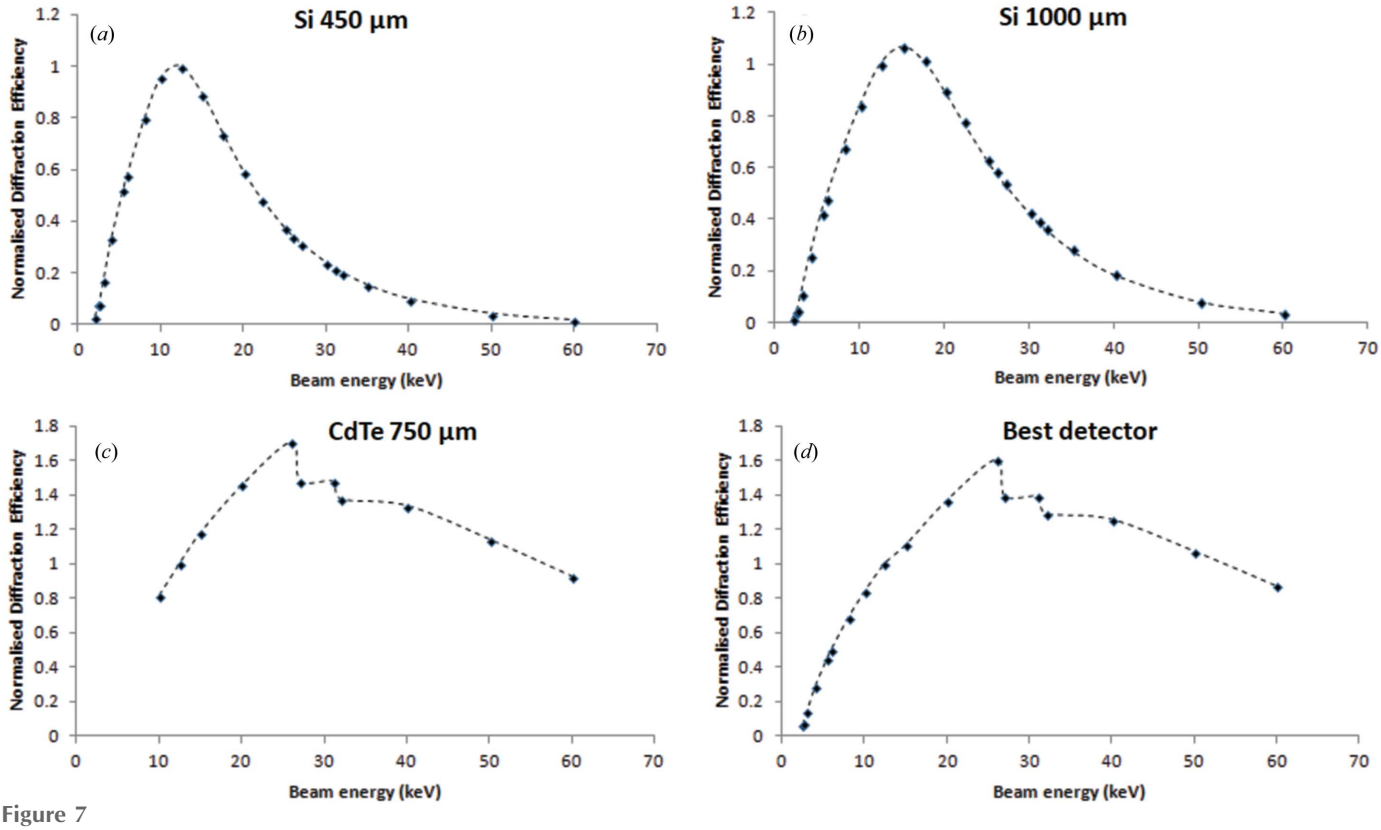

Figure 7
The diffraction efficiencies (DEs, the number of elastically scattered photons per MGy of absorbed dose), including the effects of detector quantum efficiency, at different beam energies, normalized to the value at 12.4 keV. The DE is plotted for three different sensor materials and thicknesses: (*a*) 450 µm silicon, (*b*) 1000 µm silicon and (*c*) 750 µm CdTe. The 'best detector' plot (*d*) shows the results of a calculation of the DE using the detector with the best quantum efficiency for that particular E_{inc}. This is 450 µm silicon for $E_{inc} \leq 9.3$ keV, 1000 µm silicon for 9.3 keV $< E_{inc} \leq 20$ keV, and 750 µm CdTe for $E_{inc} > 20$ keV.

photoelectron escape from the crystal is considered. When a photon is absorbed by an atom, a photoelectron is emitted with kinetic energy equal to E_{inc} minus the binding energy of that shell. Photoelectrons are mobile at cryogenic temperatures and deposit energy in the sample by inelastic collisions before thermalizing. These photoelectrons will have a finite probability of exiting the irradiated volume of the sample and reducing the absorbed dose. Several papers have considered the effects of the probability of photoelectron escape from the crystal on radiation damage rates in MX (Nave & Hill, 2005; Cowan & Nave, 2008; Sanishvili *et al.*, 2011; Fourme *et al.*, 2012; Finfrock *et al.*, 2013; Marman *et al.*, 2018) using Monte Carlo simulations and experimental verification. Accounting for photoelectron escape significantly reduces the calculated dose for microcrystals and microbeams, provided that the beam is not larger than the crystal so that the number of photoelectrons entering from the surrounding material is minimized. A reduction in the calculated absorbed dose will concomitantly increase the DE.

As E_{inc} increases, the average energy given to photoelectrons will increase so they will travel further and have an increased probability of escaping the irradiated volume. Marman *et al.* (2018) and Cowan & Nave (2008) have both used Monte Carlo simulations to demonstrate increased photoelectron escape when using higher beam energy, with Cowan & Nave suggesting that using an E_{inc} in the range 20–30 keV would provide a significant gain in DE for crystals 20 µm or less in size, provided that detectors could be optimized for this beam energy range.

Prior to the current work, the detector QE has not been included in simulations studying the effect of photoelectron escape on reducing the dose.

Here, Monte Carlo simulations were conducted using the method outlined in the supporting information and summarized in Fig. S1. These tracked the path of photons, Compton recoil electrons and photoelectrons, including photoelectrons produced in the surrounding material, to calculate the dose absorbed by the crystal. The thickness of the surrounding material is set as the maximum distance a photoelectron can travel, and hence increases as the incident beam energy rises. These simulations were used to investigate how DE changes with beam energy for microcrystals, and the results are shown in Fig. 8 for different detectors.

For silicon detectors, there is little advantage in increasing E_{inc}, irrespective of the crystal size. For a 450 µm silicon sensor, for all crystal sizes there is almost no benefit in increasing E_{inc} and for a 1000 µm silicon sensor there is still less than a factor of two improvement for crystals of 1 µm and larger. However, when using the best detector currently available, there is a greater than two-fold (ranging from two-

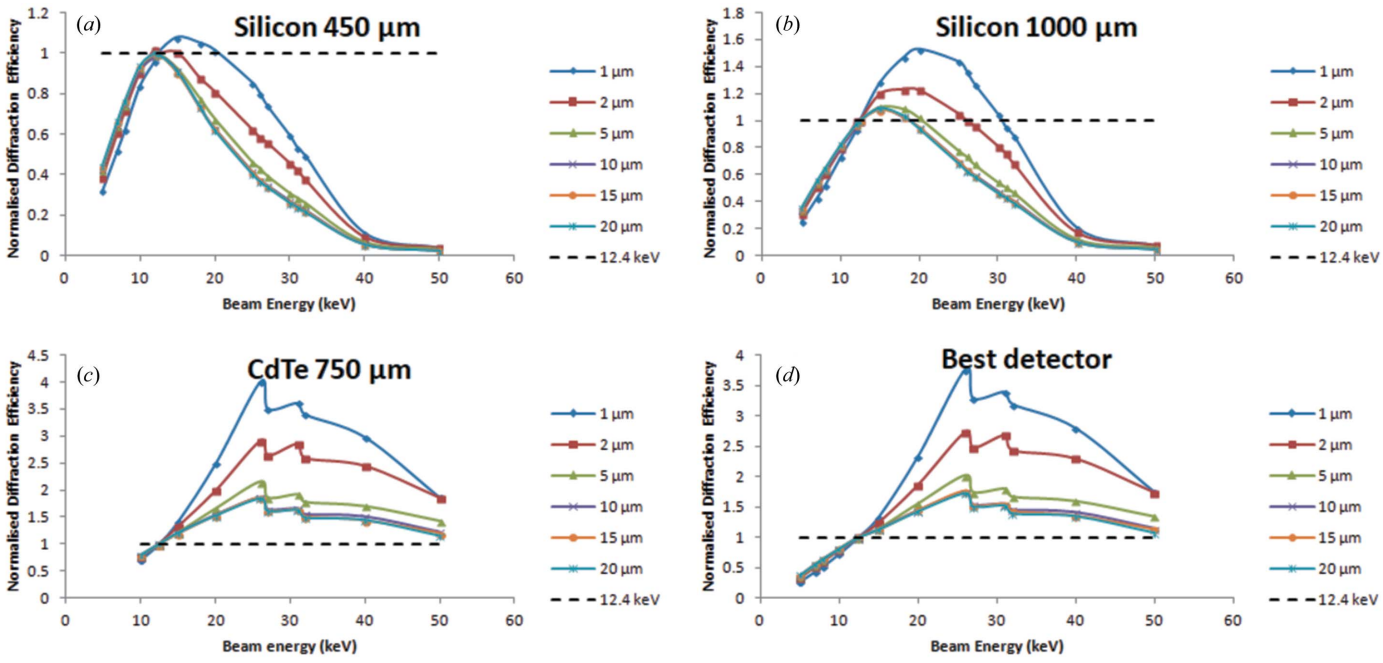

Figure 8
The changes in diffraction efficiency (including detector quantum efficiency), normalized to the value at 12.4 keV, as a function of beam energy for different cubic crystals of different sizes (specified lengths are of one crystal dimension). DE is calculated using Monte Carlo simulations including the probability of photoelectron escape from the crystal and also photoelectron entry from the surrounding material. All heavy atoms ($Z > 8$) have been removed from the crystal and the surroundings to prevent absorption edges obscuring the results. For all crystal sizes the beam is matched to the size of the crystal. The 'best detector' calculation (*d*) uses the DE for the detector which has the best quantum efficiency for that E_{inc}. This is 450 µm silicon for $E_{inc} \leq 9.3$ keV, 1000 µm for 9.3 keV $< E_{inc} \leq 20$ keV, and 750 µm CdTe for $E_{inc} > 20$ keV.

to four-fold) improvement in DE on increasing E_{inc} from 12.4 keV to 26 keV for all crystals of size 5 µm and below. For crystals 10 µm or larger, the theoretical improvement in DE becomes the same as when photoelectron escape is not included in the simulations.

The doses calculated from these simulations were also used to compute the *I*/*D* values when using the best available detector at any given E_{inc} (Fig. 9). There was a greater than factor of two improvement in *I*/*D* on increasing E_{inc} from 12.4 keV to 26 keV for: all resolutions with 1 µm crystals [Fig. 9(*a*)], resolutions of 2 Å or higher with 2 µm crystals [Fig. 9(*b*)], and 1 Å resolution with 5 µm crystals. These are lower than the predicted *I*/*D* increase from Fourme *et al.* (2012), whose Monte Carlo simulations did not include entry of photoelectrons from the surrounding material when estimating the dose.

5. Conclusions

Here we have evaluated the dependence of the diffraction efficiency on the incident X-ray energy in an MX experiment, and for the first time considered the difference made by the efficiency responses of recently available detectors. The possible escape (and entry from the surrounding material) of photoelectrons has also been considered. Monte Carlo simulations have been carried out to investigate the incident X-ray energy dependence of diffraction efficiency for microcrystals. Our results reveal a 'sweet spot' at an incident X-ray energy of 26 keV.

In general, reducing the incident beam energy (increasing the wavelength) improves experimental phasing for structure solution by enhancing the anomalous signal from S, P and first-row transition metal ions. However, although this is a generally applicable and widespread strategy, it comes at the expense of reduced diffraction efficiency. Conversely, higher beam energies up to approximately 30 keV are theoretically beneficial in MX for maximizing the amount of signal before the onset of significant radiation damage. However, for crystals and beams where photoelectron escape is of little significance (larger than 5 µm), our Monte Carlo simulations show that there is less than a factor of two improvement in DE when increasing the beam energy. Thus this is unlikely to be beneficial given that these energies reduce the magnitude of the native anomalous signal and require the use of CdTe detectors that may suffer from polarization effects.

For crystals and beams 5 µm and smaller, as E_{inc} increases there is a significant decrease in dose per diffracted photon, since photoelectron escape becomes more probable, and this enhances the advantage of going to higher E_{inc}. Raising E_{inc} from 12.4 keV to 26 keV could result in a two- to four-fold improvement in diffraction efficiency, as long as a CdTe detector is used for the 26 keV experiment. A major issue with CdTe detectors is their current lack of availability at MX beamlines, although several are being commercially manufactured (*e.g.* all sizes of EIGER detector with CdTe sensor

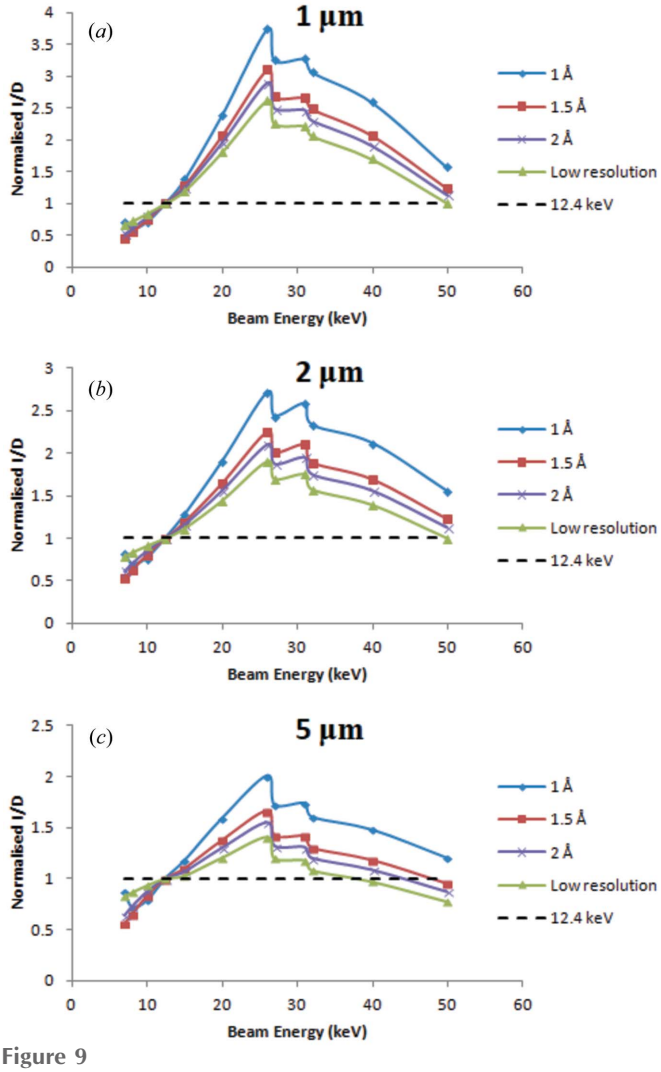

Figure 9
The changes in I/D (including detector quantum efficiency), normalized to the value at 12.4 keV, as a function of beam energy for cubic crystals of different sizes of (*a*) 1 µm, (*b*) 2 µm and (*c*) 5 µm (specified lengths are of one crystal dimension). The dose is calculated using Monte Carlo simulations including the probability of photoelectron escape from the crystal and also photoelectron entry from the surrounding material. I is calculated from equations (2) and (3). All heavy atoms ($Z > 8$) have been removed from the crystal and the surroundings to prevent absorption edges obscuring the results. For all crystal sizes the beam is matched to the size of the crystal, so the irradiated surrounding material in the beam path is in front and behind the crystal. The detector quantum efficiencies used are for the detector with the highest values for that E_{inc}. This is 450 µm silicon for $E_{inc} \leq 9.3$ keV, 1000 µm for 9.3 keV $< E_{inc} \leq 20$ keV, and 750 µm CdTe for $E_{inc} > 20$ keV.

material from DECTRIS, and the CdTe LAMBDA detector from X-Spectrum). If MX data collection with these detectors at higher energies is beneficial, they are likely to become more commonly utilized in the future. Ongoing beamline developments are underway to allow the collection of data from microcrystals using microfocus beams at beam sizes around 1 µm and at high energy, such as VMXm at Diamond Light Source (Laundy *et al.*, 2019) and FMX at NSLS-II (Fuchs *et al.*, 2016). The former beamline has the potential to reach 28 keV, and the latter is designed to allow data collection at an E_{inc} of 30 keV.

It would be extremely valuable for the clear theoretical prediction above to be validated experimentally to confirm that the results would give real benefit to structural biologists.

6. Related literature

The following references, not cited in the main body of the paper, have been cited in the supporting information: Berger *et al.* (2005); Cooper & Zare (1968); Joy (1995); Koch *et al.* (1983); Rybicki & Lightman, (1979); Salvat *et al.* (2005).

Acknowledgements

We thank Andreas Förster (DECTRIS) for providing detector quantum efficiency data on their detectors, for valuable discussions and for constructive comments on the manuscript.

References

Arndt, U. W. (1984). *J. Appl. Cryst.* **17**, 118–119.
Aurelius, O., Duman, R., El Omari, K., Mykhaylyk, V. & Wagner, A. (2017). *Nucl. Instrum. Methods Phys. Res. B*, **411**, 12–16.
Berger, M. J., Coursey, J. S., Zucker, M. A. & Chang, J. (2005). *NIST Standard Reference Database.* National Institute of Standards and Technology, Gaithersburg, MD, USA.
Berger, M. J. J., Hubbell, J. H. H., Seltzer, S. M. M., Chang, J., Coursey, J. S., Sukumar, R., Zucker, D. S. S., Cursey, J. S., Sukumar, R., Zucker, D. S. S. & Olsen, K. (1998). *XCOM: Photon Cross Section Database (version 1.5).* National Institute of Standards and Technology, Gaithersburg, MD, USA. https://www.nist.gov/pml/xcom-photon-cross-sections-database.
Bury, C. S., Brooks-Bartlett, J. C., Walsh, S. P. & Garman, E. F. (2018). *Protein Sci.* **27**, 217–228.
Bury, C. S., Carmichael, I. & Garman, E. F. (2017). *J. Synchrotron Rad.* **24**, 7–18.
Bury, C. S. & Garman, E. F. (2018). *J. Appl. Cryst.* **51**, 952–962.
Cecilia, A., Hamann, E., Haas, C., Greiffenberg, D., Danilewsky, A., Haenscke, D., Fauler, A., Zwerger, A., Buth, G., Vagovic, P., Baumbach, T. & Fiederle, M. (2011). *J. Instrum.* **6**, P10016.
Cooper, J. & Zare, R. N. (1968). *J. Chem. Phys.* **48**, 942.
Cowan, J. A. & Nave, C. (2008). *J. Synchrotron Rad.* **15**, 458–462.
Darwin, C. G. (1914). *London, Edinb. Dubl. Philos. Mag. J. Sci.* **27**, 315–333.
Darwin, C. G. (1922). *London, Edinb. Dubl. Philos. Mag. J. Sci.* **43**, 800–829.
Djinović Carugo, K., Helliwell, J. R., Stuhrmann, H. & Weiss, M. S. (2005). *J. Synchrotron Rad.* **12**, 410–419.
Donath, T., Brandstetter, S., Cibik, L., Commichau, S., Hofer, P., Krumrey, M., Lüthi, B., Marggraf, S., Müller, P., Schneebeli, M., Schulze-Briese, C. & Wernecke, J. (2013). *J. Phys. Conf. Ser.* **425**, 062001.
Finfrock, Y. Z., Stern, E. A., Alkire, R. W., Kas, J. J., Evans-Lutterodt, K., Stein, A., Duke, N., Lazarski, K. & Joachimiak, A. (2013). *Acta Cryst.* D**69**, 1463–1469.
Fourme, R., Honkimäki, V., Girard, E., Medjoubi, K., Dhaussy, A.-C. & Kahn, R. (2012). *J. Appl. Cryst.* **45**, 652–661.
Frojdh, E., Fröjdh, E., Gimenez, E. N., Krapohl, D., Maneuski, D., Norlin, B., O'Shea, V., Wilhelm, H., Tartoni, N., Thungstrom, G. & Zain, R. M. (2013). *IEEE Trans. Nucl. Sci.* **60**, 2864–2869.
Fuchs, M. R., Bhogadi, D. K., Jakoncic, J., Myers, S., Sweet, R. M., Berman, L. E., Skinner, J., Idir, M., Chubar, O., McSweeney, S. & Schneider, D. K. (2016). *AIP Conf. Proc.* **1741**, 030006.
Garman, E. F. & Weik, M. (2017). *Methods Mol. Biol.* **1607**, 467–489.
Gonzalez, A., Denny, R. & Nave, C. (1994). *Acta Cryst.* D**50**, 276–282.
Hatsui, T. & Graafsma, H. (2015). *IUCrJ*, **2**, 371–383.

Helliwell, J. R., Ealick, S., Doing, P., Irving, T. & Szebenyi, M. (1993). *Acta Cryst.* D**49**, 120–128.
Helliwell, J. R. & Fourme, R. (1983). *The ESRF as a Facility for Protein Crystallography: Report and Design Study*. ESRP Report IRI-4/83, pp. 1–36. European Science Foundation, Strasbourg, France.
Holton, J. M. (2009). *J. Synchrotron Rad.* **16**, 133–142.
Holton, J. M. & Frankel, K. A. (2010). *Acta Cryst.* D**66**, 393–408.
Homer, C., Cooper, L. & Gonzalez, A. (2011). *J. Synchrotron Rad.* **18**, 338–345.
Jakoncic, J., Di Michiel, M., Zhong, Z., Honkimaki, V., Jouanneau, Y. & Stojanoff, V. (2006). *J. Appl. Cryst.* **39**, 831–841.
Joy, D. C. (1995). *Monte Carlo Modeling for Electron Microscopy and Microanalysis.* New York: Oxford University Press.
Koch, E. E., Eastman, D. E. & Farges, Y. (1983). *Synchrotron Radiation – A Powerful Tool in Science*, in *Handbook of Synchrotron Radiation.* Amsterdam: North-Holland.
Laundy, D., Sawhney, K., Dhamgaye, V., Duller, G., Evans, G., Trincao, J. & Warren, A. (2019). *AIP Conf. Proc.* **2054**, 060006.
Lehmann, M. S., Müller, H.-H. & Stuhrmann, H. B. (1993). *Acta Cryst.* D**49**, 308–310.
Liebschner, D., Rosenbaum, G., Dauter, M. & Dauter, Z. (2015). *Acta Cryst.* D**71**, 772–778.
Liebschner, D., Yamada, Y., Matsugaki, N., Senda, M. & Senda, T. (2016). *Acta Cryst.* D**72**, 728–741.
Marman, H., Darmanin, C. & Abbey, B. (2018). *Crystals*, **8**, 267.
Mueller-Dieckmann, C., Panjikar, S., Tucker, P. A. & Weiss, M. S. (2005). *Acta Cryst.* D**61**, 1263–1272.
Nave, C. & Hill, M. A. (2005). *J. Synchrotron Rad.* **12**, 299–303.
Paithankar, K. S. & Garman, E. F. (2010). *Acta Cryst.* D**66**, 381–388.
Purohit, P., Chamberlain, D., Ruff, P. C. & Sol, M. (2016). *J. Instrum.* **11**, 12013.
Ruat, M. & Ponchut, C. (2012). *IEEE Trans. Nucl. Sci.* **59**, 2392–2401.
Rybicki, G. B. & Lightman, A. P. (1979). *Radiative Processes in Astrophysics.* New York: John Wiley & Sons, Inc.
Salvat, F., Jablonski, A. & Powell, C. J. (2005). *Comput. Phys. Commun.* **165**, 157-190.
Sanishvili, R., Yoder, D. W., Pothineni, S. B., Rosenbaum, G., Xu, S., Vogt, S., Stepanov, S., Makarov, O. A., Corcoran, S., Benn, R., Nagarajan, V., Smith, J. L. & Fischetti, R. F. (2011). *Proc. Natl Acad. Sci.* **108**, 6127–6132.
Schiltz, M., Kvick, Å., Svensson, O. S., Shepard, W., de La Fortelle, E., Prangé, T., Kahn, R., Bricogne, G. & Fourme, R. (1997). *J. Synchrotron Rad.* **4**, 287–297.
Shelley, K. L., Dixon, T. P. E., Brooks-Bartlett, J. C. & Garman, E. F. (2018). *J. Appl. Cryst.* **51**, 552–559.
Shelley, K. L. & Garman, E. F. (2019). In preparation.
Shimizu, N., Hirata, K., Hasegawa, K., Ueno, G. & Yamamoto, M. (2007). *J. Synchrotron Rad.* **14**, 4–10.
Stuhrmann, S., Bartels, K. S., Braunwarth, W., Doose, R., Dauvergne, F., Gabriel, A., Knöchel, A., Marmotti, M., Stuhrmann, H. B., Trame, C. & Lehmann, M. S. (1997). *J. Synchrotron Rad.* **4**, 298–310.
Stuhrmann, S., Hütsch, M., Trame, C., Thomas, J. & Stuhrmann, H. B. (1995). *J. Synchrotron Rad.* **2**, 83–86.
Takeda, K., Miyatake, H., Park, S.-Y., Kawamoto, M., Kamiya, N. & Miki, K. (2004). *J. Appl. Cryst.* **37**, 925–933.
Wagner, A., Duman, R., Henderson, K. & Mykhaylyk, V. (2016). *Acta Cryst.* D**72**, 430–439.
Weiss, M. S. (2017). *Methods Mol. Biol.* **1607**, 401–420.
Weiss, M. S., Panjikar, S., Mueller-Dieckmann, C. & Tucker, P. A. (2005). *J. Synchrotron Rad.* **12**, 304–309.
Zambon, P., Radicci, V., Trueb, P., Disch, C., Rissi, M., Sakhelashvili, T., Schneebeli, M. & Broennimann, C. (2018). *Nucl. Instrum. Methods Phys. Res. A*, **892**, 106–113.
Zeldin, O. B., Gerstel, M. & Garman, E. F. (2013). *J. Appl. Cryst.* **46**, 1225–1230.